University of Bristol - Explore Bristol Research

General rights

Photodissociation of S₂ (X³Σg⁻, a¹Δg, and b¹Σg⁺) in the 320−205 nm Region

Z. F. Sun,[†,§] Z. Farooq,[†,§] D. H. Parker,[*,†] P. J. J. Martin,[‡] and C. M. Western[‡]

[†]Institute for Molecules and Materials, Radboud University Nijmegen, Heyendaalseweg 135, 6525 AJ Nijmegen, The Netherlands
[‡]School of Chemistry, University of Bristol, Cantock's Close, BS8 1TS Bristol, U.K.

ABSTRACT: Photodissociation of vibrationally and electronically excited sulfur dimer molecules (S₂) has been studied in a combined experimental and computational quantum chemistry study in order to characterize bound-continuum transitions. Ab initio quantum chemistry calculations are carried out to predict the potential energy curves, spin−orbit coupling, transition moments, and bound-continuum spectra of S₂ for comparison with the experimental data. The experiment uses velocity map imaging to measure S-atom production following S₂ photoexcitation in the ultraviolet region (320−205 nm). A pulsed electric discharge in H₂S produces ground-state S₂ X³Σg⁻($v = 0−15$) as well as electronically excited singlet sulfur and b¹Σg⁺($v = 0, 1$), and evidence is presented for the production and photodissociation of S₂ a¹Δg. In a previous paper, we reported threshold photodissociation of S₂X³Σg⁻($v = 0$) in the 282−266 nm region. In the present study, S(³P$_J$) fine structure branching and angular distributions for photodissociation of S₂ (X³Σg⁻($v = 0$), a¹Δg and b¹Σg⁺) via the B″³Πu, B³Σu⁻ and 1¹Πu excited states are reported. In addition, photodissociation of the X³Σg⁻($v = 0$) state of S₂ to the second dissociation limit producing S(³P₂) + S(¹D) is characterized. The present results on S₂ photodynamics are compared to those of the well-studied electronically isovalent O₂ molecule.

S(³P₂) S(³P₁) S(³P₀)

B ← X (v=6)   B ← b(v=0,1)
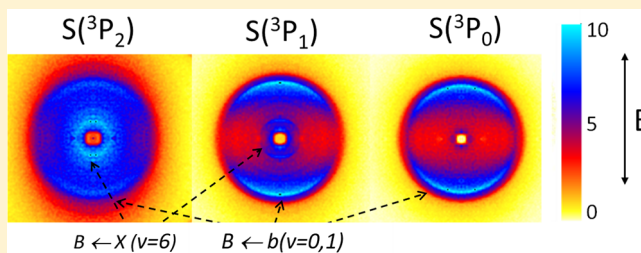
1. INTRODUCTION

The diatomic sulfur (S₂) free radical is found in many interesting environments including the atmosphere of Jupiter,[1] comet tails,[2] combustion processes,[3] volcanic activity,[4] and discharges containing sulfur compounds.[5] The presence of S₂ is usually monitored by its characteristic strong structured emission spectrum in the ultraviolet,[6−8] which is due to a transition equivalent to the B³Σu⁻ ← X³Σg⁻ Schumann−Runge transition of the isovalent O₂ molecule. Potential energy curves for the three lowest electronic states, X³Σg⁻, a¹Δg, and b¹Σg⁺, of S₂ and O₂ are shown in Figure 1 along with curves of higher electronic states relevant to this study. The combination of high symmetry and numerous valence electrons results in a large number of electronic states with few allowed transitions that connect them. In fact, there are no electric dipole-allowed transitions between any of the lowest six bound electronic states of these molecules. The strong B³Σu⁻ ← X³Σg⁻ transition of S₂ spans the wavelengths from 350 to 230 nm,[8] but below 280 nm, the sharp structures become broadened due to predissociation, with linewidths in the range[7] 6 to >20 cm⁻¹. (Pre-)dissociation by ultraviolet solar radiation, for example, is estimated[9] to limit the lifetime of S₂ in comet tails to about 250 s when the sun-comet distance is 1 AU. Most of what is known about S₂ photodissociation dynamics applies to excitation from the X³Σg⁻($v = 0$) state.[10] The goal of the present work is to improve our understanding of the photodynamics of the S₂ a¹Δg and b¹Σg⁺ and X³Σg⁻($v > 0$) states. More is known about photodissociation of the electronically isovalent O₂ molecule,[11]

which serves as a guide for understanding S₂. In particular, our recent studies on the photodissociation of electronically excited states of molecular oxygen[12,13] motivated the present study of S₂, which is probed directly after its formation in a pulsed electric discharge molecular beam, before the internally excited states have fully decayed to the ground state.

While the bound excited states and the bound−bound transitions of S₂ have been described in numerous theoretical and experimental studies, the focus here is on the allowed and forbidden bound-continuum transitions. Ab initio quantum chemistry calculations are carried out to predict the potential energy curves, spin−orbit coupling, transition moments, and bound-continuum spectra of S₂ to assist with the interpretation of the experimental data.

An important difference between S₂ and O₂ is the stronger bonding character of most S₂ bound states. The position of the B³Σu⁻ curve in S₂, for example, shifts downward in energy compared to the same state in O₂ such that bound levels are present below the first dissociation limit, which is indicated by the lower dashed horizontal line in the figure. The B″³Πu state of S₂ also shifts downward and acquires a bound character. Compared with O₂, the bound states of S₂ have a much more favorable Franck−Condon overlap (shown schematically by
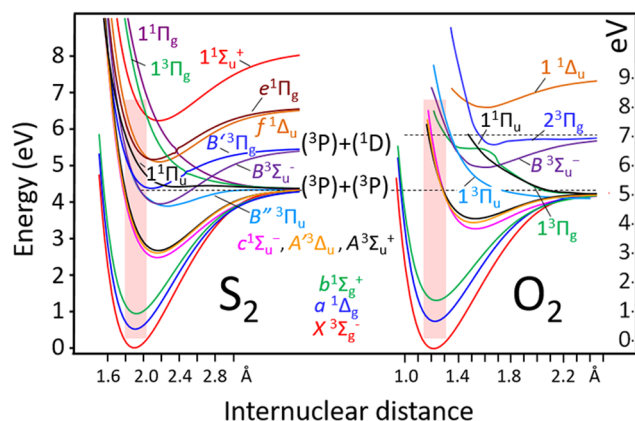
Figure 1. Potential energy curves for the lowest electronic states of S_2 from this work, and for O_2 adapted from ref 14. The two sets of curves are scaled arbitrarily on the vertical (energy) axis to the bond energy (D_0) and on the horizontal (atom−atom separation) axis to display a similar width of the ground electronic state energy well. The curves are color labeled according to their energy order at R_e, the equilibrium bond length of the ground electronic states. The horizontal dashed line indicates the first dissociation limit, and a line for the second dissociation limit is shown for O_2. The shaded rectangle indicates the region of Franck−Condon overlap. Note that O_2 shows larger interaction at the avoided crossings ($^3\Pi_g$, $^1\Pi_g$) than S_2.

shaded rectangles in Figure 1) with the lowest set of electronic states, hereafter abbreviated as X, a, and b in the UV region.

1.1. Optical Transitions of S_2. Because the lower singlet states of S_2 and O_2 are not radiatively coupled to the triplet ground state, the lowest singlet states are metastable with respect to emission. Klotz et al.[15] estimated the radiative lifetime of the S_2 $b^1\Sigma_g^+$ state to be 3.4 s and the S_2 $a^1\Delta_g$ radiative lifetime to be 350 s. The only allowed transitions starting from the ground electronic state of S_2 or O_2 are $B^3\Sigma_u^- - X^3\Sigma_g^-$ and $B''^3\Pi_u - X^3\Sigma_g^-$ (where the B″ label is specific to S_2). The equivalent $1^3\Pi_u$ upper state of molecular oxygen lacks bonding character and lies higher in energy compared to the equivalent $B''^3\Pi_u$ state of S_2, which places the $1^3\Pi_u - X^3\Sigma_g^-$ transition of O_2 in the deep vacuum ultraviolet.[8] In S_2, both allowed transitions from the X state are observed in the ultraviolet region and the transition strengths and mixing of the two bound−bound transitions has been studied in detail.[6] Starting from the S_2 a and b singlet electronic states, the allowed transitions in the UV region are $1^1\Pi_u - a^1\Delta_g$, $b^1\Sigma_g^+$; the allowed $1^1\Sigma_u^+ - b^1\Sigma_g^+$ transition lies in the VUV and has a strongly mixed Rydberg-valence character.

As pointed out by Green and Western,[6] the molecular orbital configurations of the involved electronic states are

$$B^3\Sigma_u^- \qquad\qquad 5\sigma_g^2 2\pi_u^3 2\pi_g^3,$$

$$B''^3\Pi_u, 1^1\Pi_u \qquad 5\sigma_g^2 2\pi_u^4 2\pi_g^1 5\sigma_u^1,$$

$$X^3\Sigma_g^-, a^1\Delta_g, b^1\Sigma_g^+ \quad 5\sigma_g^2 2\pi_u^4 2\pi_g^2$$

and while $B^3\Sigma_u^- - (X^3\Sigma_g^-, a^1\Delta_g, b^1\Sigma_g^+)$ are (ignoring the spin selection rules) strong bonding−antibonding $\pi_u - \pi_g$ transitions, the $\sigma_u - \pi_g$ character of the $B''^3\Pi_u$, $1^1\Pi_u - (X^3\Sigma_g^-, a^1\Delta_g,$ and $b^1\Sigma_g^+)$ transitions implies that the latter are inherently weak according to the propensity rules described by Mulliken.[16,17] Spin−orbit coupling is the main mechanism

for gaining transition strength for all forbidden transitions of O_2[18] and S_2,[15] and is stronger in S_2 compared to O_2. In addition, essentially, all of the intensity of notionally allowed the S_2 B″−X transition is known[6,19] to arise from strong but complex and indirect spin−orbit mixing of the B and B″ states. Green and Western[6,19] were able to trace out the complex mixing patterns of the two states via analysis of rotational state perturbations across the bound−bound UV absorption spectrum. This work showed that direct spin−orbit coupling of the B and B″ states is not allowed because they differ in the occupation of two separate electron orbitals; thus, the electronic spin orbit matrix element is relatively small, only 30 cm^{-1}, as compared with 200 cm^{-1} for the $B''^3\Pi_u$ state.

1.2. Photodissociation of S_2. Near-threshold photodissociation of X state S_2 into two $S(^3P)$ atoms (the lowest energy dissociation limit) with subsequent detection of $S(^3P_J; J = 2, 1,$ and 0) fragments has been reported by Frederix et al.[10] using the velocity map imaging (VMI) technique,[20] which measures the velocity (speed and angular distribution) of nascent state-selected photofragments. Rotationally cold S_2 was formed in a pulsed electric discharge of H_2S seeded in argon. An important result from this previous work was the revision of the S_2 bond energy by −396 cm^{-1} to $\overline{D_0}$ = 35 636.9 ± 2.5 cm^{-1} (4.4184 eV) with respect to the lowest rovibrational level. Dissociation of the electronically excited valence states of S_2 can lead to various different dissociation limits, with the lower energy ones tabulated in Table 1 which

Table 1. Lowest Energy Dissociation Limits of S_2

label	atomic states	energy/eV[a]
DL_1	$^3P_2 + {}^3P_2$	0
DL_2	$^3P_2 + {}^1D$	1.1454
DL_3	$^1D + {}^1D$	2.2909
DL_4	$^3P_2 + {}^1S$	2.7500
DL_5	$^1D + {}^1S$	3.8954
DL_6	$^1S + {}^1S$	5.4999

[a]Values from ref 21.

we denote DL_i, where i = 1−6. Furthermore, the fine-structure splitting of $S(^3P_J)$ is relatively large, with $E J(2, 1, 0) = (0, 0.049, 0.071$ eV), respectively. When the S-atom photofragment kinetic energy release (KER) is low (<∼1 eV), the energy resolution of VMI for a J state-detected image is sufficient to resolve the individual J' co-products. We label the lowest fine-structure component of the first dissociation limit by $DL_1(2, 2)$, where (2, 2) refers to both $S(^3P_J)$ atoms in the $J = 2$ state, and the second dissociation limit corresponds to production of $S(^3P_2 + {}^1D)$ at 1.145 eV as $DL_2(2)$. The total kinetic energy release, TKER, (=2 × KER for an S_2 molecule) is given by TKER = $E_{int} + h\nu - DL_i(J, J')$ with the parent S_2 molecule in a given electronic and vibrational (v) internal energy (E_{int}) and $h\nu$, the photon energy.

A pump-probe method was used in ref 10, where one laser dissociated the S_2 molecule and a second laser state selectively ionized nascent $S(^3P_J)$ fragments by two-photon resonance enhanced multi-photon ionization, abbreviated here as (2 + 1) REMPI. The laser used for REMPI detection of $S(^3P_J)$ alone also created extra S^+ signals that could not be assigned to $S(^3P_J)$ atom formation from one-photon dissociation of ground electronic state S_2. In the present work, we assign signals observed most easily at low laser intensity to the photo-

dissociation of singlet $b^1\Sigma_g^+$ and possibly $a^1\Delta_g$ and also describe dissociation of S_2 $X^3\Sigma_g^-$ above the second dissociation limit using two-color dissociation-detection. At high laser intensity, two-photon excitation/three-photon dissociation processes are observed and will be characterized in a separate report.

2. METHODS

2.1. Experimental Section. The experimental setup, described in detail in ref 10, consists of a source chamber (typical background pressure $\approx 10^{-7}$ mbar and 10^{-5} bar with the molecular beam operating) and a VMI detection chamber ($\sim 10^{-7}$ mbar with beam on or off). A mixture of 20% H_2S gas in argon at 2 bar was fed to a pulsed valve (Jordan) with a 0.4 mm diameter orifice. This gas expands through the nozzle into the source chamber to produce a cold, pulsed molecular beam. A stainless steel ring (4 mm diameter, 0.5 mm thickness) is mounted 2.5 mm downstream of the nozzle. At the peak of the gas pulse intensity, the voltage on the ring is pulsed to a positive high voltage (~ 1000 V) which causes an electrical discharge between the ring and grounded nozzle. The production of S_2 radicals is dependent on the width, delay, and voltage of the pulse applied to the ring. It is observed that a positive voltage (~ 1000 V, 10 μs) is more suitable for a high production rate of S_2 radicals as compared to a negative voltage (more suitable for production of SH and singlet oxygen). A tungsten filament 0.5 mm in diameter was placed adjacent to the discharge ring, and a current of around 1.5 A was passed through it. The glowing filament emits electrons that help initiate and stabilize the discharge.

S_2 molecules formed in the molecular beam are efficiently cooled in the supersonic expansion and propagate through a skimmer (2 mm diameter) 20 mm downstream from the nozzle. The beam is further collimated by a 2 mm hole in the center of the repeller electrode. In this standard VMI setup, the electrostatic lens consists of three electrodes (repeller, extractor, and ground electrode) with 20 mm inner diameter. The interaction between the molecular beam and laser beam takes place in the region between the repeller and extractor electrodes, in the detection chamber.

A frequency-doubled pulsed Nd:YAG laser (Spectra-Physics DCR-3A) operating at a repetition rate of 10 Hz is used to pump a dye laser (Spectra-Physics PDL-2) tuned to various (vacuum) wavelengths by using a range of laser dyes. The dye laser output is frequency doubled with an angle-tuned KDP/BBO crystal. About 3 to 4 mJ per pulse of polarized laser light (0.6 cm^{-1} linewidth) is focused into the interaction region using a 20 cm focal length lens. The ions created by (2 + 1) REMPI are extracted from the interaction region (between repeller and extractor) into the time-of-flight (TOF) tube. On exiting the TOF tube, the ions are detected by an imaging detector, containing a dual chevron stack of microchannel plates (MCPs) and a phosphor screen.

Mass selection is achieved by gating the voltage on the front MCP at the arrival time of the ion of interest. A charged-coupled device (CCD) camera monitoring the phosphor screen captures the ion images appearing at each laser shot. The timing for laser, discharge, detector, and valve is controlled by digital pulse generators with 10 Hz repetition rates. The CCD images are collected in a PC where the center of each event appearing in the images is registered and counted (running under Davis, LaVision). For a typical image, data are collected over 15–50k laser shots. Subsequent data analysis

includes an Abel inversion routine (using the BASEX algorithm based on a basis set expansion method[22]). The Abel inverted images contain all relevant information to extract the full three-dimensional velocity distributions (i.e., speed and angular distributions).

For kinetic energy calibration, one-color images of $S(^3P)$ detection at 308.20 nm were employed. Three strong rings appear in the S^+ image corresponding to two-photon excitation of S_2 followed by dissociation to the $^3P_2 + {}^3P_2$, $^3P_2 + {}^1D$ and $^3P_2 + {}^1S$ dissociation limits. The strong and sharp signal corresponding to ($^3P_2 + {}^1D$) production with a TKER value of 2.531 eV was used for calibration.

2.2. Theory: Ab Initio Calculations of Bound-Continuum Transitions. To estimate the strength of bound-continuum transitions for S_2, ab initio calculations of the relevant potential energy curves (shown in Figure 1) and transition moments were performed. For small molecules, such calculations can give the accuracy required for transition moments reasonably easily, as the accuracy required is much less than for energies. See, for example, ref 23, where ab initio calculations are used as the basis for calculations of absolute transition intensities.

The calculations were performed using MOLPRO 2015.1[24,25] and targeted all the S_2 singlet and triplet valence states below 50 000 cm^{-1}; above this energy Rydberg states will contribute, and the methodology used here will not capture these. This includes 25 curves overall, including two components for all Π and Δ states. The calculations were performed with the aug-cc-pV(x + d)Z basis of Dunning et al.[26] taken from the EMSL basis set exchange[27] with x = T, Q, 5 and 6. The default active space was used, consisting of the 8 orbitals arising from the 3s and 3p atomic orbitals. Initially, multiconfiguration self-consistent field (MCSCF) calculations[28,29] were performed, state averaged over the 25 states. These were followed by multireference configuration interaction calculations[30] based on the MCSCF calculations. Separate calculations were performed for each of the eight possible symmetries in the D_{2h} point group used by MOLPRO, with independent calculations for singlet and triplet states. The final energies used include the relaxed Davidson correction.[25] Transition dipole moments and spin−orbit matrix elements were also calculated, the latter using the Breit-Pauli Hamiltonian. All values were calculated from 1.4 to 5.9 Å with a step size of 0.03 Å. The ab initio potential energy curves for S_2 are shown in Figure 1, labeled by their symmetry and the spectroscopic labels as given by Huber and Herzberg in ref 31 where available; note that the $C^3\Sigma_u^-$ and higher states are not included here. Using the calculated potential energy curves, the transition dipole moments, bound state levels, and transitions were then calculated using Le Roy's LEVEL program[32] and bound continuum transitions using Le Roy's BCONT program.[33]

To investigate convergence with respect to basis set size, the energy of the potential minima of the bound states with respect to that of the $X^3\Sigma_g^-$ state were compared and found to be converged to ~ 100 cm^{-1} and typically within 250 cm^{-1} of energy differences derived from experiment. Comparison of the energies of all states calculated at a specific bond length, r, of 1.91 Å, close to the minimum of the $b^1\Sigma_g^+$ state indicated energies with respect to the $X^3\Sigma_g^-$ state converged to better than 30 cm^{-1}, spin orbit matrix elements converged to 0.1 cm^{-1}, and transition dipole moments converged to 0.003 D. Of particular interest here are the allowed and $1^1\Pi_u - b^1\Sigma_g^+$ and

$1^1\Pi_u - a^1\Delta_g$ transitions, and Figure 2 shows convergence of these two transition dipole moments. Calculation of rotational
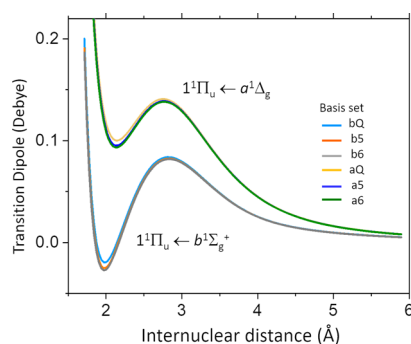

Figure 2. Transition dipole moment for the $1^1\Pi_u - b^1\Sigma_g^+$ and $1^1\Pi_u - a^1\Delta_g$ transitions for three different basis sets described in the text.

and vibrational energy levels from the calculated potential energy curves gave good results; for the ground state, vibrational intervals were within 3 cm^{-1} of the observed 720 cm^{-1} 1−0 interval, and rotational constants were within 1% of the observed values.[6] Similarly, calculating the lifetime of $v = 0$ of the $B^3\Sigma_g^-$ with respect to fluorescence to the $X^3\Sigma_g^-$ state again using the LEVEL program yields a value of 42.8 ns, in reasonable agreement with the measured lifetime of the $B^3\Sigma_g^-$ state, estimated at 32 ns for low v for levels that are not mixed with the $B''^3\Pi_u$ state.[6] Also, calculating the B−X absorption cross section gives a similarly good agreement with the measurements of Stark et al.[8]

The above suggests good results for all the ab initio intensity predictions, and given the accuracy required for the continuum calculations, we did not attempt to refine the potential energy curves. However, one of the dipole moments of particular interest here, the bound-continuum $1^1\Pi_u - b^1\Sigma_g^+$ transition is particularly weak, with a value of only 0.014 D at $r = 1.91$ Å, and the convergence is only to 0.003 D, 10% of the value. This arises because the dipole moment (shown in Figure 2) goes through zero close to this point, making the value rather sensitive to small shifts in the geometry of the states involved. The dipole moment of the $1^1\Pi_u - a^1\Delta_g$ transition (also shown in Figure 2) is 10 times larger (0.152 D) and converged to a similar absolute value and thus much better is relative terms. The $1^1\Pi_u$ state is found to be essentially repulsive but shows a shallow minimum at 2.38 Å with a barrier to dissociation of 250 cm^{-1} at 2.72 Å. This is consistent with calculations by Kiljunen et al.[34] and Swope et al.[35] though the calculations of Xing et al.[36] gave a minimum at rather longer bond length. The exact location of the minimum will be very sensitive to the details of the ab initio calculation, but it is clear from Figure 3, which shows the potential energy curves and selected wavefunctions that the absorption calculations will be insensitive to the weakly bound part of the potential. Overall, the predicted absorption coefficient for the $1^1\Pi_u - b^1\Sigma_g^+$ transition, shown as a function of wavelength in Figure 4, suggests convergence to better than 20%. (The equivalent plot for the $1^1\Pi_u - a^1\Delta_g$ transition suggests a much better convergence, <3%.)

For forbidden transitions, an effective dipole moment is calculated from the ab initio results. The dominant mechanism for inducing transitions from the $b^1\Sigma_g^+$ state is mixing with the $X^3\Sigma_g^-$ state, with the ab initio calculations predicting a matrix element of 370 cm^{-1} between states only 7970 cm^{-1} apart,
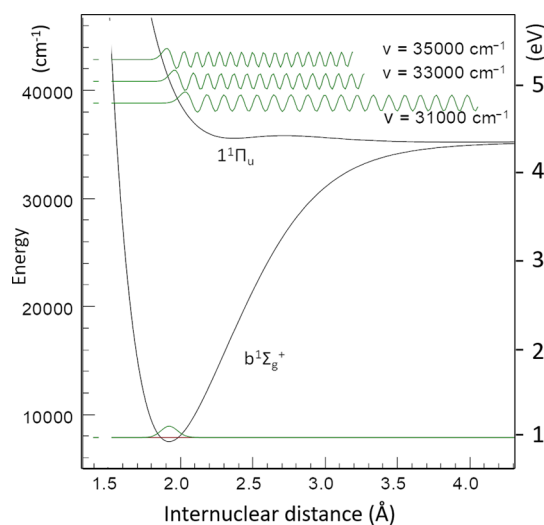
Figure 3. Potential energy curves of the $b^1\Sigma_g^+$ and $1^1\Pi_u$ states, including the $v = 0$ wavefunction for the $b^1\Sigma_g^+$ state and selected continuum wavefunctions for the $1^1\Pi_u$ state. 33 000 cm^{-1} (4.091 eV) corresponds to the peak in the absorption cross section (from the b-state).
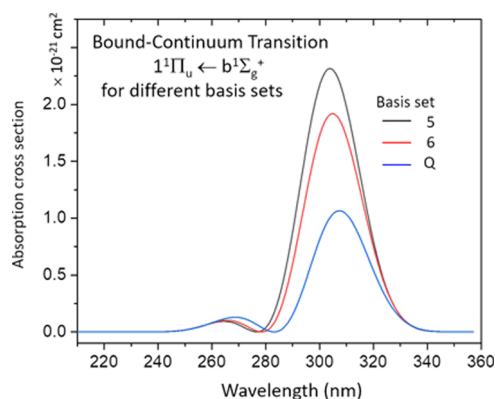
Figure 4. Absorption coefficient for the $1^1\Pi_u - b^1\Sigma_g^+$ transition as a function of wavelength, shown for three different basis sets described in the text.

implying a mixing coefficient of 0.046 from the perturbation theory. We might therefore expect to see the B−b and B″−b transitions with intensity approximately 0.2% of the respective B−X and B″−X transitions. More formally, an effective transition moment as a function of r can be calculated from the potential energy curves, transition moments, and spin−orbit coupling constants from the ab initio calculations to give expressions such as (for $b^1\Sigma_g^+$ mixed with $X^3\Sigma_g^-$ to the $B^3\Sigma_u^-$ state)

$$\langle B^3\Sigma_g^- | \mu_{eff}(r) | b^1\Sigma_g^+ \rangle \mu_{eff}(r)$$
$$= \frac{\langle X^3\Sigma_g^- | \mu | b^1\Sigma_g^+ \rangle}{E(X^3\Sigma_g^-) - E(b^1\Sigma_g^+)} \langle B^3\Sigma_g^- | \mu_{eff}(r) | b^1\Sigma_g^+ \rangle \tag{1}$$

This gives a slowly varying function with a value ≈ 0.12 D around the minimum of the b state. It diverges at large r as the energy denominator becomes small, but this is unimportant for $v = 0$. Interestingly, an alternative route, using the allowed $1^1\Sigma_u^+ - b^1\Sigma_g^+$ transition and mixing between the $1^1\Sigma_u^+$ and $B^3\Sigma_u^-$ states also contributes, though interferes destructively reducing the effective dipole moment from 0.12 to 0.08 D.

Given the high energy of this state, we are less confident as to this contribution; thus, we choose to exclude it, but it does serve to indicate the potential accuracy and limitations of the calculations. There is also a perpendicular component to the B−b transition (arising from routes via the $1^1\Pi_u$, $1^3\Pi_g$, and $B'^3\Pi_g$ states), though this is much weaker (0.0015 D). For this and all of the other states, the effective dipole is taken as a sum of the above over all routes via the states included in the ab initio calculations to the final state. This effective transition moment is plotted can then be used as for allowed transitions in the LEVEL[32] and BCONT program[33] as above.

3. RESULTS

3.1. UV Absorption and Photodissociation of S_2.
Figure 5 presents the main theoretical results of this paper:
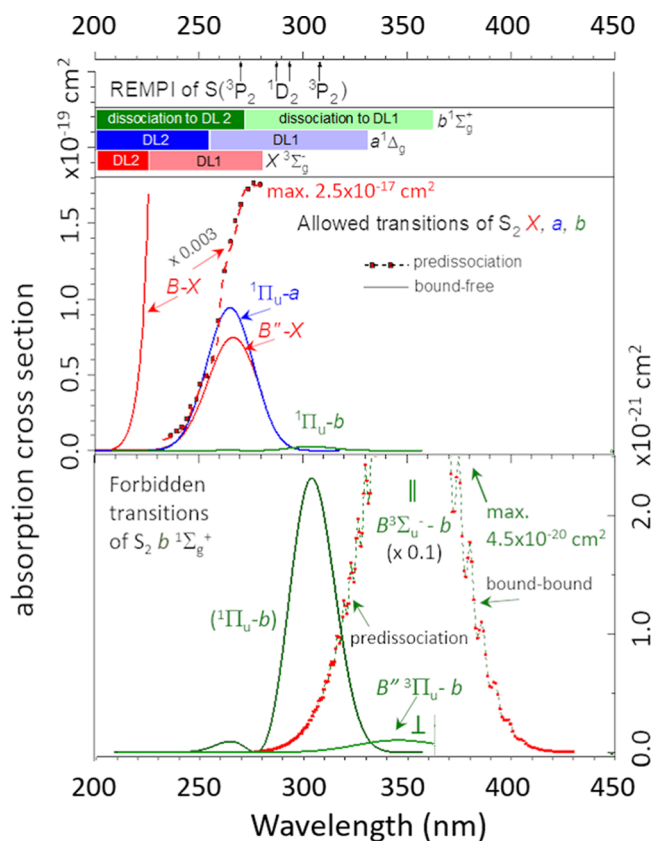
Figure 5. Calculated bound-continuum absorption spectrum of S_2 (X, a, and b). See text for details.

predictions of the state-to-state specific photoabsorption bound-continuum spectra of the allowed and forbidden UV transitions from the three lowest electronic states of S_2. Transitions from the S_2 a and b states to the S_2 Herzberg-equivalent states ($c^1\Sigma_u^-$, $A'^3\Delta_u$ and $A^3\Sigma_u^+$) lie in the visible region and are not studied in this work.

The energetic limits for dissociation from the lowest energy levels of the X, a, and b initial states are indicated in the top panel of Figure 5 in the form of horizontal bars between DL_1 and DL_2 (light shading) and above DL_2 (dark shading). Photodissociation of the ground state of S_2 to DL_1, for example, begins below 282 nm, and limit DL_2 becomes energetically accessible below 223 nm. Photodissociation from vibrationally excited levels occurs at longer wavelengths than those indicated, which are for $v = 0$. For example,

photodissociation of X($v = 5$) with $E_{int} = 0.44$ eV, which is also present in the pulsed discharge,[10] is accessible below 311.6 nm for production of two S($^3P_2$) atoms. Excitation from the X and b states to the B-state in the region between DL_1 and DL_2 leads to predissociation[6]—absorption spectra in these regions are shown with an artificial width of 300 cm^{-1} to smooth out most of the vibrational structure (consistent for B($v = 10-13$) with the results of ref 10), and the lower energy bound−bound flank of the B−b transition is also included for reference. The magnitude of the artificial width, along with the rotational temperature used in the simulation, strongly affects the structure and peak intensities of the B−X and B−b transitions in the predissociation region. Furthermore, the B-state is long-lived and can be depleted by absorption of a second photon, which is easily observed as extra rings in the S$^+$ image at laser fluxes higher than those used in this study. These factors make quantitative comparison of dissociation yield from predissociation versus direct dissociation problematic.

The most sensitive photodissociation experiment uses the same laser for both photodissociation and state-selective REMPI of the S-atom photoproducts. The positions of REMPI lines for detection of nascent S(^3P_J) and S($^1D_2$) atoms are indicated at the top horizontal axis of Figure 5 and correspond to laser wavelengths of 308.2 nm for S($^3P_2$), 310.1 nm ($^3P_1$), and 311.0 nm ($^3P_0$) via the S 4p(^3P_J) state, 269.3 for S($^3P_2$) detection via the S 5p(^3P_J) state, and 288.2 and 291.5 nm for S($^1D_2$) detection (via 4p(^1F) and 4p(^1P), respectively). Note that S(^1D) detection probes dissociation products from DL_2, whereas S(^3P) detection probes products from both limits. Direct dissociation from a specific excited state usually produces products according to the potential energy curve correlations shown in Figure 1. For example, excitation to the dissociation continuum of the $B'^3\Pi_g$ or $B^3\Sigma_u^-$ state above DL_2 (<223 nm from the X-state, <272 nm from the b-state) should produce S($^3P + ^1D$), whereas excitation below these limits produces S($^3P + ^3P$) by predissociation. Direct dissociation from the $B''^3\Pi_u$ and $1^1\Pi_u$ states from the X state below 280 nm or the a-state below 330 nm produces S($^3P + ^3P$).

Predictions of the most important UV absorption processes leading to photodissociation of S_2 are shown in the middle and lower panels of Figure 5. Four allowed transitions: B−X, B″−X, $1^1\Pi_u$−a, and $1^1\Pi_u$−b are shown, with the spectrum dominated by B−X, with the absolute cross section in cm^2 (per molecule) shown on the left vertical axis. The maximum B−X absorption, $\sigma_{max} \approx 2.5 \times 10^{-17}$ cm^2 at 281 nm under the experimental conditions of ref 8, is huge compared to the calculated $\sigma_{max} = 9 \times 10^{-20}$ cm^2 for the notionally allowed $1^1\Pi_u$−a transition at 260 nm. The lower panel of Figure 5, scaled on the right vertical axis, shows the most important forbidden dissociative transitions of S_2. Just as with O_2,[37] spin−orbit coupling of the b and X states provides transition strength for the B−b transition, which becomes predissociative below 363 nm and directly dissociates (to DL_2) below 272 nm. Coupling of the B and B″ states results in a limited transition strength for the B″−b transition. For later discussion, the allowed but weak $1^1\Pi_u$−b transition is also shown in the lower panel of Figure 5.

3.2. S-Atom Product Angular Distributions.
VMI detection of the REMPI-produced ions provides the speed and angular distribution of state-specified S-atom photofragments. Information on the optical excitation step of the photodissociation process can be predicted by theory and compared with that obtained from the photofragment angular

distribution of the photodissociation products, $I(\theta)$, which is most simply fit by

$$I(\theta) = \frac{1}{4\pi}[1 + \beta P_2(\cos\theta)] \qquad (2)$$

where $P_2(x) = \frac{1}{2}(3x^2 - 1)$ is the second-order Legendre polynomial, θ is the recoil angle with respect to the polarization axis, and β is the anisotropy parameter ($-1 < \beta < 2$). Direct photodissociation purely via a parallel transition such as B ← X ($\Sigma-\Sigma$) should yield a value of $\beta = 2$, while a perpendicular transition such as $1^1\Pi_u \leftarrow a^1\Delta_g$ or $1^1\Pi_u \leftarrow b^1\Sigma_g^+$ should yield $\beta = -1$. A measured value of β intermediate between the extremes of 2 and -1 can have several origins: a mixed transition, depolarization due to an excited state lifetime comparable to the rotational period, or a breakdown of the axial recoil approximation. For S_2, as studied here, overlapping (mixed) transitions are the mostly likely origin for intermediate values of β, and the S-atom image angular distribution reveals the amount of parallel and perpendicular characters in an electronic transition to the continuum state. Note from eq 1 that a 50:50 percentage mix of parallel and perpendicular characters yield $\beta = 0.67$.

Symmetry-forbidden transitions of S_2 that gain intensity from allowed transitions through second-order pathways involving spin−orbit coupling are characterized by their parallel and/or perpendicular character, which can vary as a function of the absorption wavelength. As indicated in Figure 5, the forbidden B−b transition is predominantly parallel, with maximum cross sections at ∼355 nm of 4.4×10^{-20} cm^2 for the parallel and 2.6×10^{-24} cm^2 for the perpendicular components. The B″−b forbidden transition in contrast is predominantly perpendicular with a maximum cross section of 1.0×10^{-22} cm^2 at ∼345 nm, while the parallel component has a maximum cross section of 2.5×10^{-24} cm^2 at ∼360 nm.

For the B−X and B−b transitions, maximum absorption occurs in the wavelength region between DL$_1$ and DL$_2$ where predissociation takes place. While the quantum yield for dissociation is unity in regions of direct dissociation, in predissociation regions the quantum yield can vary rapidly between zero and unity depending on whether the excitation is to (possibly power broadened) long lifetime bound states or the underlying continuum which is highly wavelength dependent. In our study of S_2 X-state dissociation around 280 nm, for example, the beta parameter varied between $\beta = 0$ and $\beta = 2$ within the envelope of the B($v = 12$) ← X($v = 0$) transition at ∼274 nm. Detailed modeling of this using the BETAOFNU program[38] indicated that some of this variation arose from factors such as the finite state lifetime (the width is 12 cm^{-1}) interference between P and R branch transitions. However, an underlying B″−X direct (perpendicular) dissociation was required to explain the full variation. Predissociation via the parallel B−X transition clearly competes with direct dissociation via B″−X even though the cross section is much weaker (Figure 5).

3.3. Photofragment Images. We investigate here one-photon dissociation processes in S_2 using either one laser, which drives both photodissociation and ionization, or two lasers, where the ionization laser is set typically 10−20 ns after the dissociation laser in order to avoid simultaneous excitation by both lasers. Particularly, for the one-laser experiments, it is difficult to avoid multiphoton dissociation. Below 290 nm where (2 + 1) REMPI of S_2−X becomes energetically

accessible, the number of S$^+$ channels greatly increase due to ionization of electronically excited S* atoms and to photo-dissociation of S_2^+ in a range of vibrational states. Overlap with these signals makes it difficult to distinguish one-photon dissociation. Multiphoton dissociation and ionization processes of S_2 will be described in a separate paper.

A raw velocity map image of S($^3P_2$) atoms converted by (2 + 1) REMPI to S$^+$ ions using a tightly focused laser beam at 308.2 nm is shown in Figure 6.
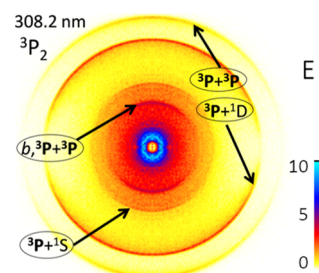
Figure 6. Raw S$^+$ image from S_2 recorded at 308.21 nm, the (2 + 1) REMPI wavelength for ionization of S$^3P_2$ atoms. The laser polarization direction E is parallel to the detector face and along the vertical axis of the figure. A color bar for conversion to signal intensity is given on the right side of the figure. For each labeled ring, the detected atom is indicated by the bold typeface.

Four rings are assigned in the image, the three outer rings correspond to two-photon dissociation of S_2 to the limits DL$_1$, DL$_2$, and DL$_3$ in decreasing radius, and the ring labeled ($^3P + ^1D$) is used to calibrate the energy scale of all other images, as mentioned in the Experimental Section. The image shown in Figure 6 was taken under typical tight-focusing conditions where a 20 cm focal length spherical lens was positioned to focus the laser beam directly at the molecular beam. By moving the focus of the laser beam 1−2 cm away from the molecular beam, one-photon dissociation signal is enhanced relative to two-photon, resulting in the three S(^3P_J), J = 2, 1, 0 images shown in Figure 7 and their corresponding TKER curves in the
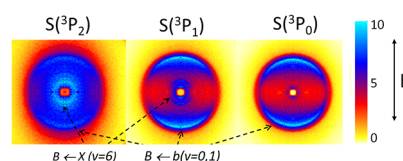
Figure 7. Raw symmetrized images of S(^3P_J) atoms taken under low laser intensity conditions near 310 nm with a short discharge time. See Figure 8 caption for more details.

0−1.0 eV TKER energy range plotted in Figure 8. Contributions near the center of the S($^3P_2$) image can arise from photodissociation of the SH molecule, which has been studied under similar discharge conditions.[39] The angular distribution of the main, outside rings in all three images is parallel with β values (Table 2) of 0.93, 0.66, and 0.62, for S(^3P_J) J = 2, 1, and 0, respectively. Beta parameters of the smaller radius rings in the S($^3P_{1,0}$) images are also listed in Table 2 according to their assignment, which is indicated on the TKER curves and explained in the analysis section.

The predicted absorption spectrum shown in Figure 5 suggests that 270 nm is a favorable wavelength to detect the S_2 a-state by photodissociation. Photodissociation of S_2 X($v = 0$)
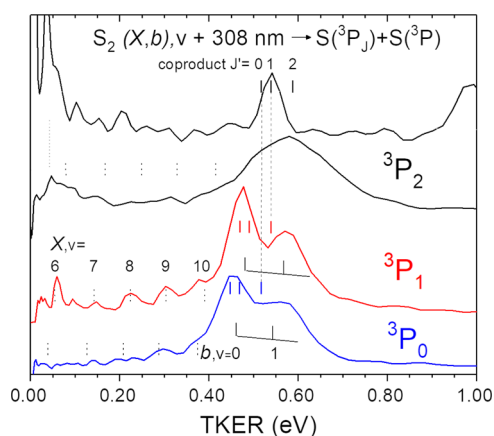
Figure 8. TKER curves for $S(^3P_J, J = 2, 1, 0)$ atoms formed from photodissociation of the S_2 molecular beam under low laser intensity conditions. Peaks seen in each TKER curve shift slower in energy due to the increasing REMPI wavelength for $J = 2$ vs 1 vs 0 detection. For dissociation of $S_2(b)$, the three vertical lines mark the energy position of the $J' = 2, 1, 0$ coproducts for each J-state detected. Vertical dashed lines in the 0.0−0.4 eV region mark the positions of the $J' = 1$ co-product for dissociation of $S_2(X, v)$. The upper trace of the S $(^3P_2)$ curves was obtained with a very short (1 μs) discharge pulse and higher laser intensity, where at higher TKER (~1 eV), signal from dissociation to DL_3 is observed (see also Figure 7). The other traces are from experiments with a short (3 μs) discharge pulse. See text for more details.

Table 2. β Values Measured in This Work for Photodissociation of S_2 $a^1\Delta_g$, $b^1\Sigma_g^+$ and $X^3\Sigma_g^-$ ($v > 5$) Around 310 nm and $X^3\Sigma_g^-$ ($v > 0$) at 205.6 nm

dissociation wavelength/nm	S atom state	$a^1\Delta_g(v = 0)$	$b^1\Sigma_g^+(v = 0)$	$X^3\Sigma_g^-$
			β	
308.2	$^3P_2$		0.93 ± 0.05	
309.9	$^3P_1$		0.66	0.65 ($v = 6$)
				0.52 ($v = 8$)
				0.55 ($v = 9$)
				0.50 ($v = 10$)
311.0	$^3P_0$		0.62	
269.2	$^3P_2$	-0.05 ± 0.1		
205.6	$^3P_2$			1.5 ± 0.5 ($v = 0$)

in this region was reported in ref 10; a more sensitive representation of that discharge beam data is shown in Figure 9.

Three TKER curves are displayed with a log intensity scale in Figure 9 for (a) 266 nm dissociation with $S(^3P_2)$ detection at 308.2 nm, (b) one-laser dissociation and 2 + 1 REMPI detection of $S(^3P_2)$ at 269.215 nm, and (c) 266 nm dissociation with $S(^3P_1)$ detection at 309.9 nm. An inverted S^+ image taken at 269.215 nm is shown in the inset using a log instead of linear color scale in order to bring up the weaker rings at larger radius. In both $S(^3P_2)$ detection images, a weak ring in the region of the $X(v = 5−6)$ dissociation signal is observed with a more isotropic angular distribution than the other observed signals. The more sensitive single-laser image yields a value of $\beta = -0.05 \pm 0.1$ for this ring. The corresponding position of this signal is indicated by a gray pattern in Figure 9 under the TKER curve of each $S(^3P_2)$
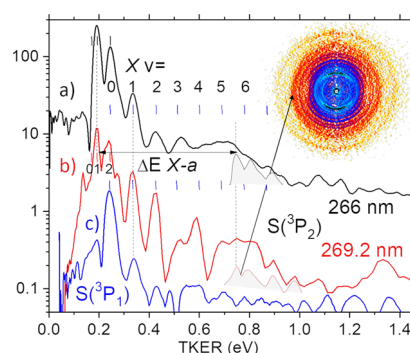

Figure 9. TKER curves using $S(^3P_{2,1})$ REMPI detection following S_2 photodissociation. (a,c) are from a two-laser experiment[10] with photodissociation at 266 nm and detection of $S(^3P_2)$ and $S(^3P_1)$ at 308.2 and 311.0 nm, respectively. Curve (b) and the inverted S^+ image shown are from a one-laser experiment[10] with dissociation and (2 + 1) REMPI of $S(^3P_2)$ at 269.215 nm. Curve (b) is shifted on the energy axis to correspond to the same photolysis energy ($\lambda = 266$ nm) as curves (a,c), and are displaced on the vertical axis for clarity. The TKER curves and the image color pattern are shown on a $\log_{10}$ scale to emphasize the weak outer ring indicated by the arrow in the figure. See text for more details.

image. The pattern is a rough trace of the X-state vibrational envelope shifted to the indicated position, which assumes similar X- and a-state vibrational distributions for the lowest v states. The relative amount of signal this extra ring corresponds to is estimated to be in the range of 1−2% of the X-state signal. The $S(^3P_1)$ image and TKER distribution for dissociation at 266 nm (and data[10] for $S(^3P_0)$—not included in Figure 9) did not show a similar signal as for $^3P_2$, within the limited signal-to-noise ratio of the experiment.

A small amount of O_2 molecules populated in the $A^3\Delta_u$ Herzberg state has been observed[13] in a pulsed O_2 discharge beam using photodissociation/$O(^1D)$ detection, where the photoproducts are formed via DL_3 (the $^1D + ^1D$ channel). For the pulsed S_2 discharge beam, single-laser dissociation/ionization experiments at 288.2 and 291.3 nm, resonant with $S(^1D)$ REMPI lines, showed no one-photon dissociation signals. While $S(^1D)$ production from S_2 (X, a, b) is not possible at this photon energy, the absence of $S(^1D)$ photoproducts indicates that there is no significant amount of population in the analogues of the Herzberg states ($c^1\Sigma_u^-$, $A^3\Delta_u$ and $A'^3\Sigma_u^+$) in the S_2 molecular beam.

A two-color image taken with a dissociation laser at 205.6 nm and detection laser at the $S(^3P_2)$ resonance at 308.2 nm is shown along with the corresponding TKER curve in Figure 10.
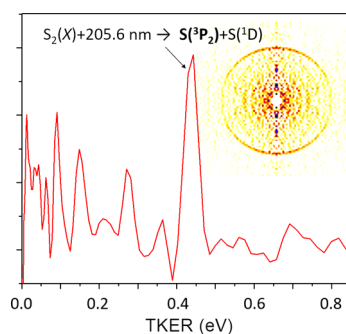
Figure 10. Background-subtracted two-color image with dissociation at 205.6 nm and detection of $S(^3P_2)$ at 308.2 nm.

Focused 205.6 nm radiation causes a very large and unstructured S^+ signal from the beam with the discharge on or off, presumably because of dissociative ionization of H_2S. While this background, particularly at low TKER, is not removed by subtraction methods, a clear ring with TKER = 0.45 eV and a strongly parallel character ($\beta = 1.5 \pm 0.5$) is observed. $S(^3P_{1,0})$ detection did not show any ring structures within the low signal-to-noise ratio of the experiment.

4. ANALYSIS AND DISCUSSION

Despite the complex chemistry of the pulsed electric discharge in a H_2S/Ar mixture with many possible sources of S^+ formation, all signals observed in this study, with the exception of the S^+ background in the two-color 205.6 dissociation/308.2 nm detection image of Figure 10, will be attributed from their TKER positions and angular distributions in this section to photodissociation of S_2 as the parent molecule. SH, predominant when using a negative high voltage discharge,[39] yields S atoms with low TKER due to the mismatch in mass of ^{32}S and ^1H. This means that regions near the center of the images (at low TKER), especially in the case of Figure 10, can be contaminated with S from SH photodissociation. It is experimentally straightforward to distinguish the detection of energetic nascent S atoms by (2 + 1) REMPI due to their wide Doppler profiles, which are evident as enhanced regions of the S^+ image along the laser propagation direction when stepping the laser across the central detection wavelength. In this case, the laser is scanned over the Doppler profile while collecting the image. Other processes that create S^+ such as dissociation of S_2^+ or ionization of excited S^* atoms are bound-continuum transitions and do not show such a Doppler effect. The sharp ring in Figure 10 and the other rings observed in the other images presented can be assigned to dissociation from various states of S_2, as discussed in this section.

4.1. Photodissociation of S_2 $X^3\Sigma_g^-$ ($v = 0$) at 205.6 nm. Inspection of Figure 5 shows that absorption of a 205.6 nm (6.030 eV) photon by the X state of S_2 should excite the molecule to the blue edge of the S_2 Schumann–Runge continuum, just above DL_2. An image of $S(^3P_2)$ fragments from excitation at this wavelength is presented in Figure 10. While the $S(^3P_2)$ signal is strongly overlapped by the photodissociation signal from H_2S present in the parent beam, one clear ring emerges at TKER = 0.45 eV, which agrees well with the expected value for dissociation to DL_2 (S^3P_2 + S^1D) limit from $h\nu - DL_1 = 6.030 - (4.418 + 1.145) = 0.467$ eV. The product angular distribution is strongly parallel, in accord with a $\Sigma - \Sigma$ transition, with $\beta = 1.5 \pm 0.5$ (Table 2) where the large uncertainty is due to the background subtraction problem. No signal was observed at 1.6 eV, the TKER is corresponding to dissociation of X($v = 0$) to DL_1, and no signal appeared near 0.5 eV above the strong background when imaging $S(^3P_{1,0})$ atoms.

Photodissociation of S_2 at 205.6 nm can be compared to photodissociation of O_2 in the Schumann–Runge continuum.[40,41] In O_2, the branching fraction to DL_2 is 99.5% with >90% of the $O(^3P_J)$ partner in $J = 2$; only 0.5% of the excited molecules produce two $O(^3P)$ atoms via DL_1. The angular distribution for the dominant DL_2 product channel is characterized by $\beta = 2.0$. Our observation that dissociation of the S_2 via the B–X transition at 205.6 nm predominantly yields measurable products at the DL_2 ($^3P_2$ + $^1D_2$) limit is then equivalent, within the large measurement uncertainty, to results for O_2.

Given our method of preparation of S_2, significant population of vibrationally excited states might be expected, and we should consider this as a possible source of signals. Photodissociation of very high levels (up to $v = 16$) of vibrationally excited ground state O_2 molecules to the DL_2 ($^3P_2$ + ^1D) limit has been observed.[12,42] Because of the large cross section of the Schumann–Runge continuum of O_2, it is possible to detect very low populations of these states. The first vibrationally excited S_2 X $v > 0$ states that can energetically access DL_2 for excitation at 310 nm is X $v = 19$ and X $v = 12$ at 268 nm. There are no obvious peaks corresponding to these signals at low KER, compared to the observed signals corresponding to DL_1 products. Absorption by singlet S_2a and b state molecules to the allowed $1^1\Pi_u$ upper state (Figure 5) does not extend to 206 nm. Observation of the photodissociation of only S_2 X $v = 0$ can thus be expected, as is observed.

4.2. Photodissociation of $S_2X^3\Sigma_g^-$ ($v > 5$) Around 310 nm. Photodissociation of S_2 in the discharge beam at the $S(^3P_J)$ REMPI detection wavelengths around 310 nm yields a series of weak but sharp rings in the TKER region below 0.5 eV (Figure 8), particularly in the $S(^3P_1)$ image. These peaks appear at TKER values expected for dissociation to the first dissociation limit. For the peak at 0.06 eV TKER labeled X($v = 6$), dissociation to the DL_1 ($^3P_2$ + $^3P_1$) limit, for example, gives $h\nu + E(v = 6) - DL_1(2, 1) = 4.00 + 0.525 - (4.418 + 0.049) = 0.053$ eV. These peaks are labeled X($v = 6-10$) in the TKER curve shown in Figure 8 for $S(^3P_1)$, and the X($v = 9$) signal is visible but weak in the $S(^3P_0)$ image and TKER curve. The energy positions of these peaks for $S(^3P_1)$ detection thus agree well with the expected positions of the $DL_1(1, 2)$ channels.

Photodissociation of X($v = 6$) at 310 nm is energetically equivalent to photodissociation of X($v = 0$) at 274 nm and thus might be expected (Figure 5) to involve excitation to the B and B″ states. It is also close to conditions used to obtain the data shown in Figure 9, where the $DL_1(1, 2)$ peak in the $S(^3P_1)$ signal is dominant. This simple pattern, compared to the $J = 2$ and 0 signals, appears to be similar for $S(^3P_1)$ detection in the X($v > 5$) signals in Figure 8. The overall intensity pattern for the set of X(v) peaks in the $^3P_1$ image in Figure 8 appears to be modulated, with a dip in intensity at X($v = 7$) for 309.9 nm excitation. This could arise from Franck–Condon effects, which are oscillatory for these values of v, though, given the discussion below, it could also arise from differences in the excitation steps.

Although the energetics suggest excitation via the strong B–X transition our previous study[10] showed that photodissociation cross sections do not increase significantly when the dissociation wavelength is resonant with the B–X bound–bound transitions. This and the varying β values measured suggest that an underlying continuum contributes to the photodissociation cross section. The obvious candidate is absorption to the B″$^3\Pi_u$–X continuum, implying a perpendicular transition. β values for peaks taken on, near, and off-resonance from the (parallel) B–X($v = 0$) peaks vary widely and nonsystematically, but taking the rough average value for $\beta = 0.6$ indicates a 50:50 mixed parallel–perpendicular dissociation, even though the B–X bound–bound absorption cross-sections are roughly a thousand times larger. The bound state channel could be reduced in intensity because of the possibility of absorption from the excited state. Excitation from X($v > 5$) is expected, and confirmed in Table 2, to give similar results for β. Predissociation of the bound B state occurs by

crossing to the B″ state, with the $1^1\Pi_u$ state possibly involved,[10] both of which correlate with the $DL_1(2, 1)$ fine structure limit consistent with adiabatic dissociation. The relatively strong $S(^3P_0)$ signal observed for both $X(v = 0)$ and $X(v > 5)$, however, shows clearly that nonadiabatic processes such as curve-crossing at long internuclear distances also play an important role.

4.3. Photodissociation of S_2 $b^1\Sigma_g^+$ Around 310 nm. When using low dissociation/REMPI laser intensity for $S(^3P_J)$ REMPI around 310 nm, strong signals are observed (Figure 8) around 0.5 eV TKER. From the relative total intensity of the $S(^3P_J)$ $J = 2, 1$ and 0 detection images shown in Figure 7, it is found that $J = 1$ and 0 are formed in significant fractions in the dissociation process, i.e., the $(2, 2)$ channel is not the dominant product. Use of a very short $(1~\mu s)$ electric discharge pulse (upper trace of Figure 8, for the image shown in Figure 7) appears to result in the best vibrational cooling, where a peak at TKER $= 0.54$ eV is found. The predicted TKER for 308.20 nm dissociation of the b-state to $DL_1(2, 1)$ is TKER $= h\nu + E_{int}(b) - DL_1(2, 1) = 4.0226 + 0.989 - (4.4184 + 0.0491) = 0.544$ eV, where E_{int} for the b-state is taken from the recent electron photodetachment imaging study of Qin et al.,[43] which are consistent with the earlier spectroscopic study of Fink et al.[44] The lower three TKER curves in Figure 8 use a 3 μs discharge length, and both the $S(^3P_1)$ and $S(^3P_0)$ curves show a clear extra peak higher by 0.08 eV which corresponds to the photodissociation of $b(v = 1)$. The $^3P_1$ and $^3P_0$ curves show extra peaks due to photodissociation of $S_2X^3\Sigma_g^-(v > 5)$, as discussed earlier in this section. Because of their slightly longer REMPI wavelengths, the $S(^3P_1)$ and $S(^3P_0)$ curves shift to progressively lower TKER than the $S(^3P_2)$ curve, with peaks corresponding to $DL_1(1, 1)$ and $DL_1(0, 1)$, respectively. The energy resolution is not sufficient to eliminate contributions from channels involving the $S(^3P_0)$ coproduct. The $S(^3P_0)$ detection curve peaks between the energy position of $DL_1(0, 0)$ and $(0, 1)$. The angular distribution for the main peak in the TKER curves for of all three images is parallel with β values (Table 2) of 0.93, 0.66, and 0.62, for $S(^3P_J)$ $J = 2, 1$, and 0, respectively.

Photodissociation of the O_2 b state has been found to pass exclusively through the second dissociation limit via the spin-forbidden B ← b continuum,[45] which has, for example, a cross section of 10^{-22} cm^2 around 225 nm.[37,46] As seen in Figure 5, direct and perpendicular dissociation of S_2 to DL_1 via the allowed $1^1\Pi_u$ ← b and the spin-forbidden B″ ← b transitions are possible along with predissociation via the parallel, spin-forbidden B ← b transition. Unusually, the spin-forbidden B−b transition is much stronger than the spin-allowed transition, which is seen from Figure 2 to arise from a transition moment going through zero. At 310 nm, the B ← b transition is roughly 10 times stronger than the $1^1\Pi_u$ ← b transition, and the B″−b transition is weaker than both, so probably does not contribute. Because the measured beta values (Table 2) for b-state photodissociation are in the range of 0.6−0.93, this indicates a roughly equal mixture of parallel and perpendicular transition, suggesting a similar situation as for the X state dissociation discussed above with a competition between two channels, in this case, B and $1^1\Pi_u$ rather than B and B″. Given the uncertainty in the $1^1\Pi_u$ ← b transition moment noted above, it is not possible to be more quantitative.

4.4. Photodissociation of the S_2 $a^1\Delta_g$ State Around 270 nm. The predicted TKER for 266 nm dissociation of the a-state to $DL_1(2, 1)$ is TKER $= h\nu + E_{int} - DL_1(2, 1) = 4.661$ + 0.545 − (4.4184 + 0.0491) = 0.739 eV, where E_{int} for the a state is taken from the spectroscopic study of Setzer et al.[47] This corresponds well with the position of the broad peak marked by an arrow in the image shown in Figure 9 for the $S(^3P_2)$ images taken at the dissociation wavelengths 266 and 269.2 nm (where the TKER curve for the later wavelength is shifted to correspond to the energy equivalent of 266 nm). The ring indicated in Figure 9 has $\beta = -0.05$ (Table 2). The only predicted absorption process starting from the S_2 a-state (Figure 5) is via the dipole-allowed but weak $1^1\Pi_u$ ← $a^1\Delta_g$ transition which has a maximum around 260 nm (Figure 5); no spin-forbidden transitions with any appreciable cross-section are predicted. The transition should thus be purely perpendicular ($\beta = -1$). However, the measured β value is likely to be contaminated by overlap with stronger peaks from the photodissociation of $X(v = 5−9)$ which, as discussed above, are found to have more positive beta values; so, the $1^1\Pi_u$ ← a transition is the most likely candidate for the absorption.

In contrast, photodissociation of the O_2 a-state takes place through the spin-forbidden $A'^3\Delta_u$ ← $a^1\Delta_g$ Chamberlain transition, which has a mainly parallel character.[12]

5. CONCLUSION

Photodissociation imaging is shown to be a suitable means for detecting the presence of S_2 in various excited states. Detection of S_2 $X(v = 0)$ in the 266−282 nm region was described in ref 10, and this paper demonstrates efficient detection of the S_2 b-state by photodissociation at the $S(^3P_J)$ atom REMPI wavelengths around 310 nm and detection of S_2 $X(v > 0)$ by photodissociation in both the 266 and 310 nm regions. Detection of the lowest energy singlet metastable S_2 a-state at 266 nm is more tentative, presumably due to a much smaller population of molecules in this state, which is also indicated in previous studies of S_2 formed in several types of discharge systems. In all of the above cases, dissociation mainly takes place via the lowest dissociation limit producing $S(^3P_2)$ + $S(^3P_1)$ products. At the dissociation wavelengths studied, the absorption spectrum is dominated by the predissociative part of the B−X transition, which is equivalent to the O_2 Schumann−Runge continuum. Based on the observed angular distributions, the contribution from B predissociation appears to be low, possibly because of removal of B-state by further photoexcitation.

In comparison with O_2, the presence of the $1^1\Pi_u$ and B″$^3\Pi_u$ states at the studied dissociation wavelengths allow dissociation to the first limit, producing mainly, but not exclusively, $S(^3P_2)$ + $S(^3P_1)$ products. Direct excitation of S_2 into the B−X continuum produces results quite similar to those from the isovalent O_2 molecule.

■ ASSOCIATED CONTENT

Special Issue Paper

This paper was intended for the "Hanna Reisler Festschrift Virtual Special Issue", published August 1, 2019.

■ AUTHOR INFORMATION

Corresponding Author

*E-mail: parker@science.ru.nl.

ORCID ●

D. H. Parker: 0000-0003-0297-168X

■ REFERENCES

(1) Noll, K.; McGrath, M.; Trafton, L.; Atreya, S.; Caldwell, J.; Weaver, H.; Yelle, R.; Barnet, C.; Edgington, S. HST spectroscopic observations of Jupiter after the collision of comet Shoemaker-Levy 9. *Science* **1995**, *267*, 1307−1313.

(2) Calmonte, U.; Tzou, C.-Y.; Balsiger, H.; Le Roy, L.; Gasc, S.; Sémon, T.; Rubin, M.; Altwegg, K.; Bieler, A.; Hässig, M.; Wampfler, S. F.; Berthelier, J. J.; Gombosi, T. I.; Dhooghe, F.; Cessateur, G.; van Dishoeck, E. F.; Fiethe, B.; Fuselier, S. A. Sulphur-bearing species in the coma of comet 67P/Churyumov−Gerasimenko. *Mon. Not. R. Astron. Soc.* **2016**, *462*, S253−S273.

(3) Fowler, A.; Vaidya, W. M. The Spectrum of the Flame of Carbon Disulphide. *Proc. R. Soc. A* **1931**, *132*, 310−330.

(4) Spencer, J. R.; Jessup, K. L.; McGrath, M. A.; Ballester, G. E.; Yelle, R. Discovery of Gaseous S_2 in Io's Pele Plume. *Science* **2000**, *288*, 1208−1210.

(5) Lakshminarayana, G.; Mahajan, C. G. Spectroscopic studies of the sulphur afterglow. *J. Quant. Spectrosc. Radiat. Transfer* **1976**, *16*, 549−552.

(6) Green, M. E.; Western, C. M. A deperturbation analysis of the B $3\Sigma u-$ ($v'=0-6$) and th B″ $3\Pi u$($v'=2-12$) states of S_2. *J. Chem. Phys.* **1996**, *104*, 848.

(7) Wheeler, M. D.; Newman, S. M.; Orr-Ewing, A. J. Predissociation of the B $3\Sigma u-$ state of S_2. *J. Chem. Phys.* **1998**, *108*, 6594−6605.

(8) Stark, G.; Herde, H.; Lyons, J. R.; Heays, A. N.; de Oliveira, N.; Nave, G.; Lewis, B. R.; Gibson, S. T. Fourier-transform-spectroscopic photoabsorption cross sections and oscillator strengths for the S_2 B$\Sigma u-3-X\Sigma g-3$ system. *J. Chem. Phys.* **2018**, *148*, 244302.

(9) De Almeida, A. A.; Singh, P. D. Photodissociation lifetime of $32S2$ molecule in comets. *Earth, Moon, Planets* **1986**, *36*, 117−125.

(10) Frederix, P. W. J. M.; Yang, C.-H.; Groenenboom, G. C.; Parker, D. H.; Alnama, K.; Western, C. M.; Orr-Ewing, A. J. Photodissociation Imaging of Diatomic Sulfur (S_2)†. *J. Phys. Chem. A* **2009**, *113*, 14995−15005.

(11) Parker, D. H. Laser photochemistry of molecular oxygen. *Acc. Chem. Res.* **2000**, *33*, 563−571.

(12) Farooq, Z.; Chestakov, D. A.; Yan, B.; Groenenboom, G. C.; van der Zande, W. J.; Parker, D. H. Photodissociation of singlet oxygen in the UV region. *Phys. Chem. Chem. Phys.* **2014**, *16*, 3305−3316.

(13) Scheidsbach, R. J. A.; Parker, D. H. Detection of the O2 A′$3\Delta U$ Herzberg III state by photofragment imaging. *Phys. Chem. Chem. Phys.* **2019**, *21*, 14278.

(14) Saxon, R. P.; Liu, B. Ab initio configuration interaction study of the valence states of O2. *J. Chem. Phys.* **1977**, *67*, 5432−5441.

(15) Klotz, R.; Marian, C. M.; Peyerimhoff, S. D.; Hess, B. A.; Buenker, R. J. Calculation of spin-forbidden radiative transitions using correlated wavefunctions: Lifetimes of b1Σ+, a1Δ states in O2, S2 and SO. *Chem. Phys.* **1984**, *89*, 223−236.

(16) Mulliken, R. S. Intensities of Electronic Transitions in Molecular Spectra II. Charge-Transfer Spectra. *J. Chem. Phys.* **1939**, *7*, 20−34.

(17) Mulliken, R. S. Intensities of Electronic Transitions in Molecular Spectra IX. Calculations on the Long Wave-Length Halogen Spectra. *J. Chem. Phys.* **1940**, *8*, 234−243.

(18) Klotz, R.; Peyerimhoff, S. D. Theoretical study of the intensity of the spin- or dipole forbidden transitions between the c 1$\sum$- u, A′ 3Δ u, A 3$\sum$+ u and X 3$\sum$- g, a 1Δ g, b 1$\sum$+ g states in O2. *Mol. Phys.* **1986**, *57*, 573−594.

(19) Green, M. E.; Western, C. M. Upper vibrational states of the B″3Πu state of 32S2. *J. Chem. Soc., Faraday Trans.* **1997**, *93*, 365−372.

(20) Eppink, A. T. J. B.; Parker, D. H. Velocity map imaging of ions and electrons using electrostatic lenses: Application in photoelectron and photofragment ion imaging of molecular oxygen. *Rev. Sci. Instrum.* **1997**, *68*, 3477−3484.

(21) Kramida, A.; Ralchenko, Y.; Reader, J.; Team, N. A. *Atomic Spectra Database; NIST Atomic Spectra Database* version 5.2; National Institute of Standards and Technology: Gaithersburg, MD, 2013; p 20899.

(22) Dribinski, V.; Ossadtchi, A.; Mandelshtam, V. A.; Reisler, H. Reconstruction of Abel-transformable images: The Gaussian basis-set expansion Abel transform method. *Rev. Sci. Instrum.* **2002**, *73*, 2634.

(23) Brooke, J. S. A.; Bernath, P. F.; Western, C. M.; Sneden, C.; Afşar, M.; Li, G.; Gordon, I. E. Line strengths of rovibrational and rotational transitions in theX2Πground state of OH. *J. Quant. Spectrosc. Radiat. Transfer* **2016**, *168*, 142−157.

(24) Werner, H.-J.; Knowles, P. J.; Knizia, G.; Manby, F. R.; Schütz, M. Molpro: a general-purpose quantum chemistry program package. *Wiley Interdiscip. Rev.: Comput. Mol. Sci.* **2012**, *2*, 242−253.

(25) Werner, H.-J.; Knowles, P. J.; Knizia, G.; Manby, F. R.; Schütz, M.; Celani, P.; Györffy, W.; Korona, T.; Lindh, R.; Mitrushenkov, A.; Rauhut, G.; Shamasundar, K. R.; Adler, T. B.; Amos, R. D.; Bernhardsson, A.; Berning, A.; Cooper, D. L.; Deegan, M. J. O.; Dobbyn, A. J.; Eckert, F.; Goll, E.; Hampel, C.; Hesselmann, A.; Hetzer, G.; Hrenar, T.; Jansen, G.; Köppl, C.; Liu, Y.; Lloyd, A. W.; Mata, R. A.; May, A. J.; McNicholas, S. J.; Meyer, W.; Mura, M. E.; Nicklass, A.; O'Neill, D. P.; Palmieri, P.; Pflüger, K.; Pitzer, R.; Reiher, M.; Shiozaki, T.; Stoll, H.; Stone, A. J.; Tarroni, R.; Thorsteinsson, T.; Wang, M.; Wolf, A. MOLPRO version 2015.1, a package of ab initio programs see http://www.molpro.net, 2015.

(26) Dunning, T. H.; Peterson, K. A.; Wilson, A. K. Gaussian basis sets for use in correlated molecular calculations. X. The atoms aluminum through argon revisited. *J. Chem. Phys.* **2001**, *114*, 9244−9253.

(27) Schuchardt, K. L.; Didier, B. T.; Elsethagen, T.; Sun, L.; Gurumoorthi, V.; Chase, J.; Li, J.; Windus, T. L. Basis Set Exchange: A Community Database for Computational Sciences. *J. Chem. Inf. Model.* **2007**, *47*, 1045−1052.

(28) Werner, H. J.; Knowles, P. J. A second order multiconfiguration SCF procedure with optimum convergence. *J. Chem. Phys.* **1985**, *82*, 5053−5063.

(29) Knowles, P. J.; Werner, H.-J. An efficient second-order MC SCF method for long configuration expansions. *Chem. Phys. Lett.* **1985**, *115*, 259−267.

(30) Werner, H.-J.; Knowles, P. J. An efficient internally contracted multiconfiguration-reference configuration interaction method. *J. Chem. Phys.* **1988**, *89*, 5803−5814.

(31) Linstrom, P. J.; Mallard, W. *NIST Chemistry Webbook; NIST Standard Reference Database No. 69*, 2001.

(32) Le Roy, R. J. LEVEL: A computer program for solving the radial Schrödinger equation for bound and quasibound levels. *J. Quant. Spectrosc. Radiat. Transfer* **2017**, *186*, 167−178.

(33) Le Roy, R. J.; Kraemer, G. T. *BCONT 2.2 A Computer Program for Calculating Bound−Continuum Transition Intensities for Diatomic Molecules*; University of Waterloo Chemical Physics Research Report CP-650R^2; University of Waterloo, 2004.

(34) Kiljunen, T.; Eloranta, J.; Kunttu, H.; Khriachtchev, L.; Pettersson, M.; Räsänen, M. Electronic structure and short-range recombination dynamics of S2 in solid argon. *J. Chem. Phys.* **2000**, *112*, 7475−7483.

(35) Swope, W. C.; Lee, Y.-P.; Schaefer, H. F. Diatomic sulfur: Low lying bound molecular electronic states of S2. *J. Chem. Phys.* **1979**, *70*, 947.

(36) Xing, W.; Shi, D.; Sun, J.; Liu, H.; Zhu, Z. Extensive ab initio study of the electronic states of S2 molecule including spin-orbit coupling. *Mol. Phys.* **2013**, *111*, 673−685.

(37) Lewis, B. R.; Gibson, S. T.; Slanger, T. G.; Huestis, D. L. The B $3\Sigma u - \leftarrow b$ $1\Sigma g+$ transition of molecular oxygen. *J. Chem. Phys.* **1999**, *110*, 11129−11132.

(38) Kim, H.; Dooley, K. S.; Groenenboom, G. C.; North, S. W. Vibrational state-dependent predissociation dynamics of ClO (A2Π3/2): Insight from correlated fine structure branching ratios. *Phys. Chem. Chem. Phys.* **2006**, *8*, 2964−2971.

(39) Rose, R. A.; Orr-Ewing, A. J.; Yang, C.-H.; Vidma, K.; Groenenboom, G. C.; Parker, D. H. Photodissociation dynamics of the A $\Sigma 2+$ state of SH and SD radicals. *J. Chem. Phys.* **2009**, *130*, 034307.

(40) Huang, Y. L.; Gordon, R. J. The multiplet state distribution of O(3PJ) produced in the photodissociation of O2 at 157 nm. *J. Chem. Phys.* **1991**, *94*, 2640−2647.

(41) Wu, S.-M.; Radenovic, D. Č.; van der Zande, W. J.; Groenenboom, G. C.; Parker, D. H.; Vallance, C.; Zare, R. N. Control and imaging of O(1D2) precession. *Nat. Chem.* **2011**, *3*, 28−33.

(42) Wu, S.-M.; Chestakov, D.; Groenenboom, G. C.; van der Zande, W. J.; Parker, D. H.; Wu, G.; Yang, X.; Vallance, C. Angular momentum polarisation in the O(1D) products of O2 photolysis via the B state. *Mol. Phys.* **2010**, *108*, 1145−1157.

(43) Qin, Z.; Wang, L.; Cong, R.; Jiao, C.; Zheng, X.; Cui, Z.; Tang, Z. Spectroscopic identification of the low-lying electronic states of S2 molecule. *J. Chem. Phys.* **2019**, *150*, 044302.

(44) Fink, E. H.; Kruse, H.; Ramsay, D. A. The high-resolution emission spectrum of S2 in the near infrared: The b1Σg+-X3Σg− system. *J. Mol. Spectrosc.* **1986**, *119*, 377−387.

(45) Eppink, A. T. J. B.; Parker, D. H.; Janssen, M. H. M.; Buijsse, B.; van der Zande, W. J. Production of maximally aligned O(1D) atoms from two-step photodissociation of molecular oxygen. *J. Chem. Phys.* **1998**, *108*, 1305−1308.

(46) Minaev, B. F.; Telyatnik, L. G. Ab initio calculation of transition dipole moments for transitions between valence states in oxygen molecules. *Opt. Spectrosc.* **2001**, *91*, 883−890.

(47) Setzer, K. D.; Kalb, M.; Fink, E. H. The a1Δg→X3Σ−g magnetic dipole transition of S2. *J. Mol. Spectrosc.* **2003**, *221*, 127−130.